RSC Advances

PAPER

View Article Online
View Journal | View Issue

Cite this: *RSC Adv.*, 2017, **7**, 6911

Core–shell superparamagnetic monodisperse nanospheres based on amino-functionalized $CoFe_2O_4$@SiO_2 for removal of heavy metals from aqueous solutions†

Chunrong Ren,[a] Xingeng Ding,*[ab] Huiqin Fu,[a] Wenqi Li,[a] Huating Wu[a] and Hui Yang[ab]

Received 4th December 2016
Accepted 4th January 2017

DOI: 10.1039/c6ra27728d

www.rsc.org/advances

To remove heavy metals from aqueous solutions, amino-functionalized superparamagnetic $CoFe_2O_4$@SiO_2 ($CoFe_2O_4$@SiO_2–NH_2) core–shell nanospheres were designed and constructed. In particular, well-defined $CoFe_2O_4$ nanoparticles (NPs) were synthesized by reverse co-precipitation. The shell of the $CoFe_2O_4$ NPs was composed of amorphous silica (SiO_2), which had a thickness of ~35 nm. Monodisperse $CoFe_2O_4$@SiO_2 nanospheres grafted with more amino groups had a greater adsorption capacity and higher removal efficiency for heavy metal ions (Cd(II): 199.9 mg g^{-1}, 99.96%; Cu(II): 177.8 mg g^{-1}, 88.05%; Pb(II): 181.6 mg g^{-1}, 90.79%). The effects of the pH, initial concentrations, reaction temperature and time on the adsorption of heavy metal ions by $CoFe_2O_4$@SiO_2–NH_2 were analyzed systematically. The adsorption process on the nanospheres was well described by the Langmuir model. The adsorption kinetics can be best fitted by the pseudo-second-order kinetics model. Analysis of a thermodynamic study of Cu(II) showed that the process of adsorption is spontaneous and endothermic in nature. Owing to the superparamagnetic properties with a high saturation magnetization value (32.92 emu g^{-1}) of $CoFe_2O_4$@SiO_2–NH_2, the metal-loaded nanospheres can be quickly removed from an aqueous solution (30 s) by magnetic separation. Moreover, the nanospheres exhibited good reusability for up to five cycles. The results confirm that the monodisperse amino-functionalized $CoFe_2O_4$@SiO_2 magnetic nanospheres could be a potential adsorbent for the effective and regenerable removal of heavy metals from aqueous solutions.

1 Introduction

Water pollution caused by heavy metals has been one of the most serious worldwide environmental issues in recent years.[1–4] Heavy metals can cause a variety of negative effects on human health even at low dosages. A suitable method is needed for the removal and preconcentration of heavy metal ions. Several methods have been developed for the treatment of heavy metals such as membrane separation, ion exchange, chemical precipitation, solvent extraction, adsorption, *etc.*[5–7] Among these, adsorption is considered to be an attractive approach owing to its simplicity, high efficiency and the fact that it does not yield harmful by-products.[8–11] Up to now, various adsorbents have been developed for the removal of different heavy metal ions.[12–17] However, the development of adsorbents with high adsorption capacity, fast adsorption–desorption kinetics, easy separation and recyclability is extremely challenging. Therefore, the design and fabrication of a novel adsorbent with good adsorption capacity and convenient separation and regeneration are of both scientific and technological importance.

Recently, magnetic separation has been considered to be an effective technique for separating adsorbents from wastewater; therefore, magnetic adsorbents have been investigated widely.[18–23] Moreover, magnetic adsorbents with a core–shell structure have attracted much interest owing to their enhanced properties and the synergistic effect between multiple discrete components. Specifically, the magnetic core can facilitate rapid separation, and the functional shell can adsorb heavy metal ions quickly. Many research studies have been carried out on the preparation of diverse core–shell magnetic composites.[24–31] For instance, monodisperse Fe_3O_4/SiO_2 magnetic nanoparticles were prepared by a sonochemical method.[32,33] An amino-functionalized Fe_3O_4@SiO_2 core–shell magnetic nanomaterial as an effective and recyclable adsorbent was synthesized,[34–38] and the method of functionalization was post-modification[34–36] or co-condensation.[37,38] Venkateswarlu *et al.*[27] presented novel Fe_3O_4@DAPF core–shell ferromagnetic nanorods for the removal of Pb(II) from aqueous solutions, which had adsorption

[a]*Department of Materials Science and Engineering, Zhejiang University, Hangzhou 310027, China. E-mail: msedxg@zju.edu.cn*

[b]*Zhejiang California International Nano Systems Institute, Hangzhou 310027, China*

† Electronic supplementary information (ESI) available. See DOI: 10.1039/c6ra27728d

capacities (83.3 mg g^{-1}) comparable to the highest previous value. Zhang *et al.*[38] fabricated Fe_3O_4@SiO_2–NH_2 core–shell nanoparticles *via* a controllable sol–gel process. The nanoparticles enabled easy recovery by an external magnet and effective removal of Pb(II) (q_m = 243.9 mg g^{-1}, 25 °C). Furthermore, Yuan *et al.*[39] prepared a novel multifunctional microsphere with a large-pore-size mesoporous silica shell and a magnetic core (Fe_3O_4), which can graft more amino groups and adsorb more heavy metals in aqueous solution (Pb(II): 880.6 mg g^{-1}, Cu(II): 628.3 mg g^{-1}, Cd(II): 492.4 mg g^{-1}). Among core–shell magnetic composites, the use of Fe_3O_4 nanoparticles (NPs) as the core has been widely studied owing to their unique magnetic properties. However, the chemical stability of Fe_3O_4 is fairly poor, even it is coated by a protective layer.

$CoFe_2O_4$ NPs have some advantages such as moderate saturation magnetization,[40–42] easy preparation, and rapid separation,[43,44] and especially their high chemical and corrosion stability. Recently, Zhao *et al.*[45] introduced a $CoFe_2O_4$–zeolite material for adsorbing gallium and indium. Thiol-functionalized silica-coated $CoFe_2O_4$ magnetic composites with a core–shell structure have been synthesized and can potentially be applied to remove Pb(II) or Hg(II) ions in water.[46,47] However, there are few reports concerning the preparation of monodisperse superparamagnetic $CoFe_2O_4$@SiO_2 nanocomposites by a simple and low-cost method. Some cobalt–ferrite composites were relatively agglomerated and had larger sizes,[48] which restricted their adsorption properties.

Here, we demonstrate a modified method of designing monodisperse magnetic nanospheres with a core–shell structure. The synthesized $CoFe_2O_4$@SiO_2–NH_2 nanospheres were used as an effective adsorbent to remove heavy metal ions (Cu(II), Cd(II), and Pb(II)) from aqueous solutions. The effects of the solution pH, reaction temperature, reaction time and initial concentration of Cu(II) on the adsorption performance were examined. In addition, the adsorption kinetics, thermodynamics and reusability of the adsorbents were also investigated. The adsorption and regeneration processes of the adsorbent are presented in Fig. 1d–i. These novel monodisperse nanospheres show great potential to be used as an excellent, economic, and regenerable adsorbent for the removal of heavy metal ions.

2 Experiments

2.1 Materials

3-Aminopropyltriethoxysilane (APTES) was obtained from Aladdin Chemical Reagent Co., Ltd. $Fe(NO_3)_3 \cdot 9H_2O$, $Co(NO_3)_2 \cdot 6H_2O$, $Cu(NO_3)_2 \cdot 3H_2O$, $Cd(NO_3)_2 \cdot 4H_2O$, $Pb(NO_3)_2$, sodium hydroxide (NaOH), polyethylene glycol (PEG), ammonium hydroxide ($NH_3 \cdot H_2O$, 25%), *o*-xylene, citric acid, ethanol and tetraethyl orthosilicate (TEOS) were purchased from Sinopharm Chemical Reagent Co., Ltd. All reagents were of analytical grade and were used without further purification. Deionized water was used in all the experiments.

2.2 Preparation of $CoFe_2O_4$ (CFO) magnetic nanoparticles

CFO NPs were synthesized *via* an improved reverse co-precipitation method. Firstly, $Fe(NO_3)_3 \cdot 9H_2O$ (8.08 g) and $Co(NO_3)_2 \cdot 6H_2O$ (2.91 g) in a molar ratio of 2 : 1 were dissolved in 100 mL deionized water and stirred at 70 °C. This solution

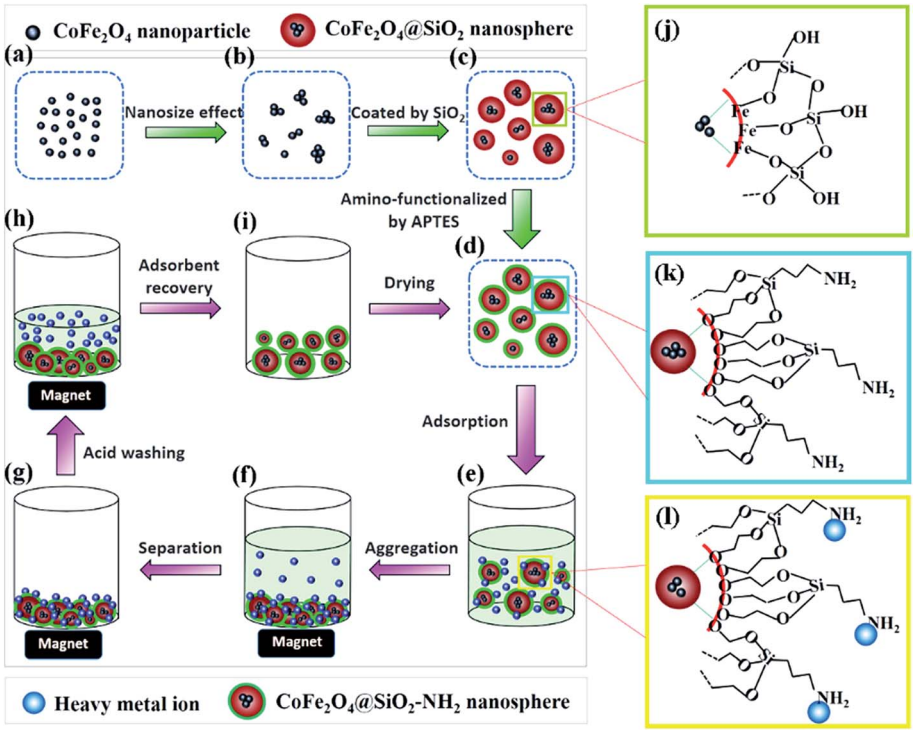

Fig. 1 Schematic illustration of the synthetic procedure of $CoFe_2O_4$@SiO_2–NH_2 core–shell nanospheres (a–d, j and k) and the adsorption and regeneration process of heavy metals (d–i and l).

was marked as solution A. Secondly, PEG (6000) as a dispersant was added to 150 mL ammonium hydroxide ($NH_3 \cdot H_2O$, 2.0 M) under vigorous stirring at 70 °C. This solution was marked as solution B. Thirdly, solution A was added dropwise to solution B under stirring for 1 h. The mixed solutions were refluxed for 2 h under the conditions of a boiling water bath. Fourthly, the resulting black precipitate was magnetically separated, washed with deionized water until the pH reached 7, dried in a vacuum at 80 °C for 12 h, and subsequently sintered at 350 °C for 12 h to drive out residual carbon. Finally, the prepared CFO magnetic NPs (0.3 g) were dispersed *via* sonication in 200 mL citric acid solution (0.1 M). The magnetic NPs that were modified by citric acid were collected by magnetic separation, washed three times with ethanol, dispersed in a mixture of ethanol (200 mL) and deionized water (50 mL) by sonication for 2 h, and stored in a 500 mL vial until further use. This solution was marked as solution C.

2.3 Preparation of $CoFe_2O_4$@SiO_2 (CFO@SiO_2) magnetic nanospheres

CFO@SiO_2 nanospheres were synthesized according to a previously reported method.[48] Typically, $NH_3 \cdot H_2O$ was added to solution C to adjust its pH value. When the pH reached ~9, TEOS (3 mL) was added dropwise to the suspension slowly under sonication. Afterward, the mixture was mechanically stirred for 12 h at room temperature. The resulting powder was collected by a magnet, washed with deionized water until neutral (pH = 7), and dried in a vacuum at 80 °C for 12 h.

2.4 Preparation of amino-functionalized $CoFe_2O_4$@SiO_2 (CFO@SiO_2–NH_2)

In order to ensure anhydrous conditions, CFO@SiO_2 (2.0 g) was washed with 80 mL *o*-xylene. After magnetic separation and dispersion in 150 mL *o*-xylene, the solution was stirred at 50 °C for 1 h. Subsequently, APTES (8 mL) was added to the above suspension dropwise. The mixture was refluxed at 100 °C for 24 h under mechanical stirring. The resulting black product was isolated by magnetic separation, washed with ethanol, and dried in a vacuum at 80 °C for 12 h.

2.5 Characterization

The structure and morphology of CFO, CFO@SiO_2 and CFO@SiO_2–NH_2 were investigated by scanning electron microscopy (SEM; SU-70), transmission electron microscopy (TEM; Philips CM200), and high-resolution transmission electron microscopy (HRTEM; Tecnai G2 F20 S-TWIN FEI). All samples for TEM measurements were deposited on a carbon film supported by copper grids. The crystal structures of the samples were characterized by powder X-ray diffraction (XRD; PANalytical X'Pert PRO) with Cu Kα radiation ($\lambda = 1.5418$ Å). The diffraction data were collected over the angle range of 10–80° with a step size of 0.02°. Fourier transform infrared spectra (FT-IR) were recorded using KBr pellets with a Nicolet 5700 spectrometer. XPS data were obtained with an electron spectrometer (ESCALAB 250Xi) using monochromatized Al Kα radiation ($h\nu = 1486.6$ eV). The specific magnetization of the powders was also measured as a function of the applied magnetic field at room temperature using a vibrating-sample magnetometer (VSM 7407). The concentrations of metal ions were determined by atomic adsorption spectroscopy (AAS; AAnalyst 800).

2.6 Batch adsorption experiments

The effects of the pH, initial concentration, reaction time and temperature on the adsorption of heavy metals onto CFO@SiO_2–NH_2 (0.4 g L^{-1}) were examined using a batch technique. The pH values were adjusted from 4 to 7 using NaOH (0.1 M) or HCl (0.1 M). Meanwhile, the concentrations of $Cu(NO_3)_2$ (80 mg L^{-1}) and the adsorbent (20 mg) were kept constant. $Cu(NO_3)_2$ solutions with a range of initial ion concentrations of 20–320 mg L^{-1} were investigated, and the experiment was conducted at a pH of 7 and 35 °C. In order to study the effect of the contact temperature, CFO@SiO_2–NH_2 (20 mg) was added to 50 mL of 80 mg L^{-1} $Cu(NO_3)_2$ solution (pH 7) at different contact temperatures (25 °C, 35 °C, 45 °C, and 55 °C). The effect of the reaction time on the adsorption of heavy metal ions (Cd(II), Cu(II), and Pb(II)) by CFO@SiO_2–NH_2 was studied. Solutions of heavy metal ions (50 mL, 80 mg L^{-1}) containing adsorbents (20 mg) were shaken for different periods of time (from 0 to 780 min) at a pH of 7 and 35 °C. The removal efficiency (R_e (%)) and the adsorption capacity (mg g^{-1}) of CFO@SiO_2–NH_2 for heavy metal ions were calculated by the following equations:

$$R_e(\%) = \frac{C_0 - C_t}{C_0} \times 100 \quad (1)$$

$$q_t = \frac{(C_0 - C_t)V}{m} \quad (2)$$

$$R_e(\%) = \frac{C_0 - C_e}{C_0} \times 100 \quad (3)$$

$$q_e = \frac{(C_0 - C_e)V}{m} \quad (4)$$

where C_0, C_t and C_e (mg L^{-1}) are the concentrations of the ions initially, at time t and at equilibrium, respectively, and q_t and q_e are the adsorption capacities at time t and at equilibrium, respectively. V is the volume of the adsorbate (L), and m is the mass of the adsorbent (g).

2.7 Regeneration studies

Cd(II), Cu(II) and Pb(II) ions were desorbed by washing the adsorbed $CoFe_2O_4$@SiO_2–NH_2 (20 mg) with 50 mL HCl (0.1 M), respectively. The mixture was stirred continuously in a shaker at 100 rpm for 12 h at 35 °C, and then the concentration of each heavy metal ion in the solution was calculated. The resulting CFO@SiO_2–NH_2 was used in the next adsorption cycle after being washed and dried.

3 Results and discussion

3.1 Formation mechanism of $CoFe_2O_4$@SiO_2–NH_2 nanospheres

Fig. 1 illustrates the synthesis process of $CoFe_2O_4$@SiO_2–NH_2 nanospheres. Firstly, Fe^{3+} and Co^{2+} ions co-precipitate to form $CoFe_2O_4$ NPs under alkaline conditions (Fig. 1a). The $CoFe_2O_4$ nanocrystals aggregate to some extent owing to the nanoeffect (Fig. 1b). After being modified with citric acid, the obtained $CoFe_2O_4$ ferrofluids can be dispersed homogeneously in water (Fig. 1b). Secondly, Si–OH groups obtained from the hydrolysis of TEOS can interact with Fe–OH groups on the surface of $CoFe_2O_4$ NPs, and then monodisperse $CoFe_2O_4$@SiO_2 nanospheres with core–shell structures are formed (Fig. 1c and j). Lastly, silanol groups (Si–OH) on the surface of $CoFe_2O_4$@SiO_2 react with methyl groups (–CH_3) from APTES, which results in amino groups exposed to the outside of $CoFe_2O_4$@SiO_2 (Fig. 1d and k). The proposed structures of $CoFe_2O_4$@SiO_2 and $CoFe_2O_4$@SiO_2–NH_2 are presented in Fig. 1j and k, respectively. To confirm the above mechanism, the results of SEM, TEM, XRD and FT-IR analyses are shown in Section 3.2.

3.2 Morphological and structural analysis

The detailed morphological and structural features of pure $CoFe_2O_4$, $CoFe_2O_4$@SiO_2, and $CoFe_2O_4$@SiO_2–NH_2 were examined by SEM and TEM (Fig. 2). Bare $CoFe_2O_4$ particles with an average diameter of approximately 10 nm were aggregates composed of a few crystalline grains (Fig. 2d). After being coated with a non-porous silica layer, an obvious core–shell structure can be observed for all the CFO@SiO_2 nanospheres, with an electron-dense (dark contrast) $CoFe_2O_4$ core and an electron-lean amorphous SiO_2 shell (light contrast). The shells were homogeneous and uniform with a mean thickness of ~35 nm (Fig. 2e). The subsequent amino-functionalization process had no influence on the shape and particle size of $CoFe_2O_4$@SiO_2–NH_2 nanospheres (Fig. 2f and g), in comparison with CFO@SiO_2. In Fig. 2, panels (a), (b) and (c) display typical SEM images of CFO NPs, CFO@SiO_2 and CFO@SiO_2–NH_2 nanospheres, respectively. They illustrate that the composites were well dispersed with near-spherical morphology. To investigate the structural details of the cores, HRTEM studies were performed for CFO@SiO_2–NH_2 (Fig. 2h and i). It was found that there were well-resolved lattice planes in the core of the nanospheres. The result of a fast Fourier transform (FFT) showed that the lattice fringes corresponding to an interplanar distance of ~2.506 Å can be attributed to the (311) planes of a $CoFe_2O_4$ phase (Fig. 2i, inset). Hence, it is clear that CFO is located in the central part of the particle and amorphous SiO_2 is homogeneously distributed throughout the whole nanosphere.

The phase purity and crystal structure of CFO, CFO@SiO_2, and CFO@SiO_2–NH_2 were determined by XRD (Fig. S1a, ESI†). The diffraction peaks of all samples can be easily indexed to an inverse spinel structure, which matches well with the value in JCPDS no. 01-1121, indicating the formation of a $CoFe_2O_4$ phase. The average particle size calculated using the Debye–Scherrer formula from the reflection peak of the (311) planes was about 10 nm, which is consistent with the result measured from the HRTEM image (Fig. 2i). For comparison, an additional broad peak appeared at a 2θ value of 20–28° (red line, blue line),

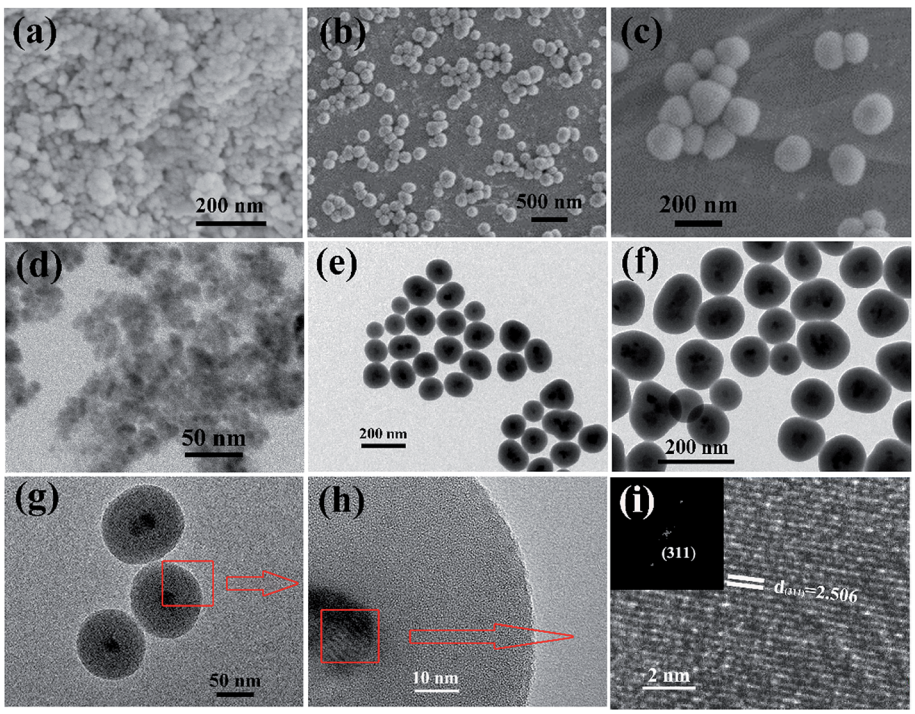

Fig. 2 SEM and TEM images of (a and d) CFO NPs, (b and e) CFO@SiO_2, and (c, f and g) CFO@SiO_2–NH_2 nanospheres. (h and i) HRTEM images of CFO@SiO_2–NH_2 nanospheres. (Inset of (i)) fast Fourier transform (FFT) pattern.

which could correspond to amorphous SiO_2. Furthermore, owing to the coating of a silica shell on the surface of CFO NPs,[26,49,50] the intensity of the XRD diffraction peaks of CFO@SiO_2 and CFO@SiO_2–NH_2 exhibited a slight decrease. As can be seen, the above results confirm the formation of $CoFe_2O_4$ and $CoFe_2O_4$@SiO_2.

To determine the chemical composition of the samples, FT-IR spectroscopy was carried out (Fig. S1b†). The bands at 882 and 602 cm^{-1} for bare $CoFe_2O_4$ were attributed to Co–O and Fe–O vibrations, respectively, and decreased for CFO@SiO_2 and CFO@SiO_2–NH_2. This demonstrates that $CoFe_2O_4$ is in the interior of the composites. The bands at 3440 and 1633 cm^{-1} in all the spectra were assigned to the stretching and bending vibrations of O–H groups of water.[34] In comparison with CFO, new peaks at 1092, 799 and 468 cm^{-1} were observed in the spectra of CFO@SiO_2 and CFO@SiO_2–NH_2, which correspond to the typical symmetric and bending vibrations of Si–O–Si,[51–54] respectively. The spectrum of CFO@SiO_2–NH_2 nearly possessed the same characteristic bands as CFO@SiO_2 except for the decreased intensity of the absorption of free silanol groups at 946 cm^{-1} (ref. 35 and 55) and the broadened peak at 1092 cm^{-1}. In addition, new bands around 1563–1340 cm^{-1} were detected for CFO@SiO_2–NH_2, which can be assigned to the stretching and bending vibrations of amino groups from APTES. X-ray photoelectron spectrometry (XPS) was carried out to further analyze the surface composition of CFO@SiO_2 and CFO@SiO_2–NH_2 nanospheres (Fig. S4†). A N 1s peak was only observed for CFO@SiO_2–NH_2 at 399.3 eV. All results are in good agreement with the proposed structure of CFO@SiO_2 and CFO@SiO_2–NH_2 (Fig. 1j and k) and also show that the silica shell was amino-functionalized successfully.

3.3 Magnetic properties

Superparamagnetic properties of adsorbents are critical for their practical application. When exposed to a magnetic field, the particles display strong magnetization, but without retaining any magnetism after the removal of the applied magnetic field. Superparamagnetism can prevent them from aggregating in water. Fig. 3b shows magnetic hysteresis loops for CFO NPs, CFO@SiO_2 and CFO@SiO_2–NH_2 core–shell nanospheres. It is apparent that they all displayed superparamagnetic behavior owing to the nanometer-sized $CoFe_2O_4$ particles in the core. The saturation magnetization values were measured to be 50.07, 36.10 and 32.92 emu g^{-1} for CFO NPs, CFO@SiO_2 and CFO@SiO_2–NH_2 core–shell nanospheres, respectively. The decrease in saturation magnetization was related to the surface of CFO being covered by SiO_2 and functionalized by APTES. The CFO@SiO_2–NH_2 core–shell composites can be dispersed in water with slight shaking, which results in a black suspension (0 s). Upon placement of a magnet beside a vial, the materials were quickly attracted to one side of the vial within a few seconds (30 s), leaving the solution transparent. Dynamic pictures are shown in Fig. 3a, and the materials could be well redispersed by shaking once the magnetic field was removed. On the basis of the above magnetism analysis, the amino-functionalized CFO@SiO_2 that we prepared would have great potential applications in recycling of the adsorbent.

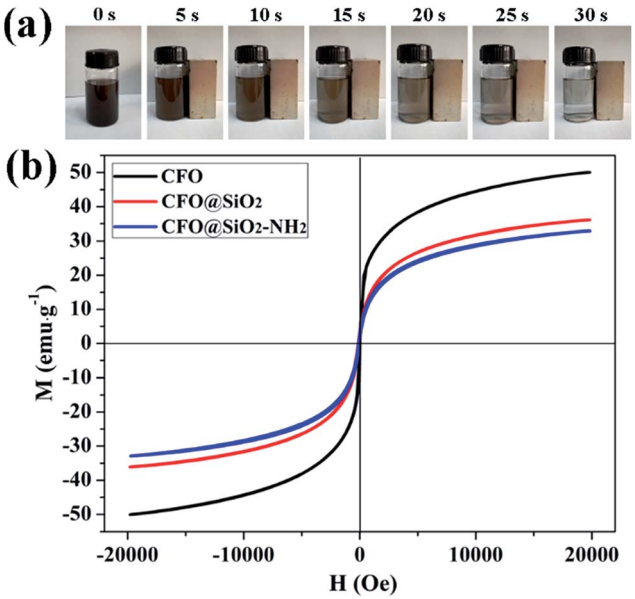

Fig. 3 (a) Dynamic pictures of magnetic separation process of CFO@SiO_2–NH_2 and (b) room-temperature (300 K) magnetic hysteresis loops of CFO, CFO@SiO_2, and CFO@SiO_2–NH_2.

3.4 Adsorption studies of the amino-functionalized core–shell nanospheres (CFO@SiO_2–NH_2)

3.4.1 Effect of pH on adsorption of Cu(II) by CFO@SiO_2–NH_2. The pH is an important factor in the process of adsorption. Experiments were performed at different pH values ranging from 4 to 7, because precipitation of the metal hydroxide may occur when the pH is higher than 7. With an increase in the pH value, the removal efficiency increased from 3.5% to 88.05% (Fig. 4a), and the adsorption capacity increased from 7.0 to 192.02 mg g^{-1} (Fig. 4b). The results show that the adsorption capacity of CFO@SiO_2–NH_2 nanospheres toward the heavy metal ions is strong under near-neutral conditions and poor in the highly acidic pH region. At a low pH, H^+ ions compete with Cu^{2+} ions over CFO@SiO_2–NH_2, which reduces the extent of adsorption. In addition, coulombic repulsion is present between Cu^{2+} ions and protonated amine groups ($-NH_3^+$). As the pH value increased, an increase in the number of $-NH_2$ sites on the surface of the adsorbents resulted in the adsorption of more copper ions. Thus, the maximum adsorption level was observed at a pH of 7 (Fig. 4).

3.4.2 Effect of initial concentration on adsorption of Cu(II) by CFO@SiO_2–NH_2 and study of adsorption isotherms. The effect of the initial concentration of the metal ions on adsorption was investigated *via* isotherms, which can provide fundamental information on how adsorbents interact with adsorbates.[56] Fig. 5 shows the adsorption of Cu(II) on CFO@SiO_2–NH_2 as a function of its initial concentration (from 20 to 320 mg L^{-1}). With an increase in the initial concentration of Cu(II) ions, the adsorption capacity of CFO@SiO_2–NH_2 displayed a continuous improvement (Fig. 5a). When the initial concentration was increased to 240 mg L^{-1}, there was no further increase in capacity. The maximum adsorption capacity for

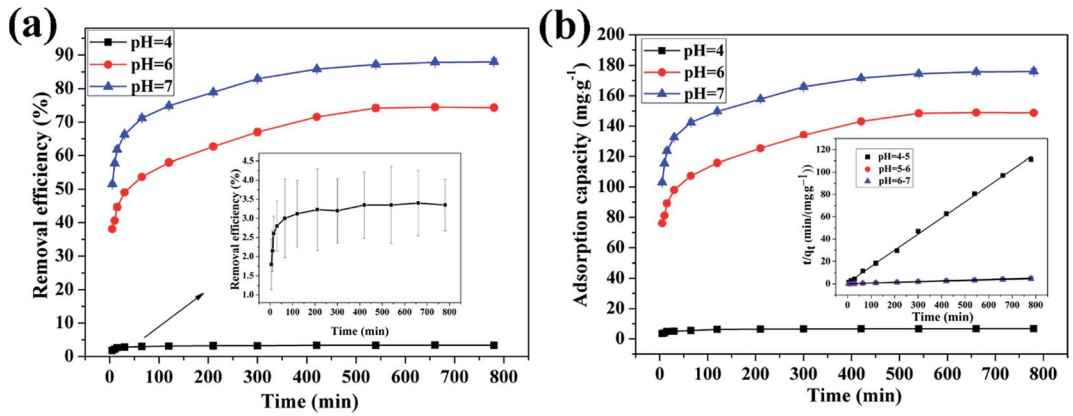

Fig. 4 Effect of pH on adsorption of Cu(II) by CFO@SiO_2–NH_2: (a) removal efficiency, (b) adsorption capacity, and (inset of b) pseudo-second-order kinetics plots.

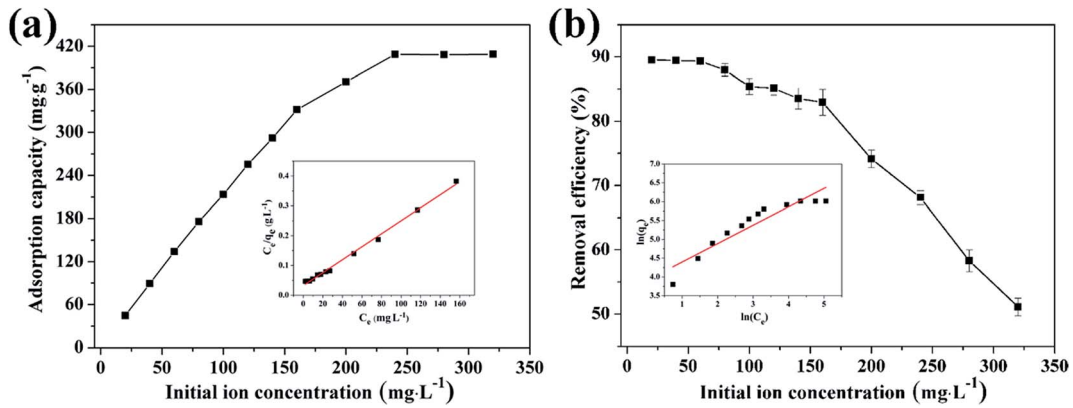

Fig. 5 Effect of initial concentration on adsorption of Cu(II) by CFO@SiO_2–NH_2: (a) adsorption capacity, (inset of (a)) Langmuir isotherm plot, (b) removal efficiency, and (inset of (b)) Freundlich isotherm plot.

Cu(II) was 408.75 mg g^{-1}, which was higher than our previous result. Cu(II) ions could be almost completely removed at an initial concentration of 60 mg L^{-1} and lower (Fig. 5b). On a further increase in the initial concentration to 320 mg L^{-1}, the removal efficiency gradually decreased. This fact indicates that Cu(II) ions filled the surface space of $CoFe_2O_4$@SiO_2–NH_2 at the critical concentration,[31] which resulted in a decline in the removal efficiency at higher concentrations.

The insets of Fig. 5a and b illustrate the Langmuir and Freundlich isotherm plots, respectively. The corresponding parameters of these models are given in Table 1. The equilibrium sorption data were fitted well to the Langmuir isotherm, yielding a correlation coefficient of $R^2 = 0.9956$. The relation between C_e/q_e and C_e displayed good linearity, and thus the adsorption of Cu(II) on CFO@SiO_2–NH_2 can be regarded as a monolayer adsorption process. In other words, the adsorption process occurred at the sites of amino groups on the surface of CFO@SiO_2–NH_2. The calculated maximum adsorption capacity for Cu(II) was 410.72 mg g^{-1}, which approximated to the experimental value. The essential characteristic of the Langmuir isotherm can be expressed in terms of the constant separation factor R_L, which is also shown in Table 1. The value of R_L indicates that the shape of the isotherm is either unfavorable ($R_L > 1$), linear ($R_L = 1$), favorable ($0 < R_L < 1$), or irreversible ($R_L = 0$). The value of R_L for the adsorbent was 0.1425 (between 0 and 1), which confirms that the adsorption is a favorable process.

3.4.3 Effect of reaction temperature on adsorption of Cu(II) by CFO@SiO_2–NH_2 and study of adsorption thermodynamics. Fig. 6 shows the effect of temperature on the adsorption of Cu(II) by CFO@SiO_2–NH_2. At the beginning, the adsorption rate increased upon an increase in the reaction temperature. The adsorption capacity increased from 166.94 mg g^{-1} (35 °C) to 187.48 mg g^{-1} (55 °C), and the removal efficiency accordingly rose from 83.47% (35 °C) to 93.74% (55 °C). This can be explained by the fact that adsorbed ions move much faster at a high temperature. Then, the contact area between the adsorbent and the metal ions increases, which results in increases in the adsorption capacity and removal efficiency of the adsorbent for metal ions.

In order to obtain in-depth information on the inherent energetic changes that are associated with adsorption, the thermodynamic parameters were estimated. The changes in Gibbs energy (ΔG°), enthalpy (ΔH°), and entropy (ΔS°) can be calculated from the following equations:

Table 1 Parameters of Langmuir and Freundlich adsorption isotherms for Cu(II) on CFO@SiO_2–NH_2

Model	Equation	Parameters			
		q_m (mg g^{-1})	b (L g^{-1})	R^2	R_L
Langmuir 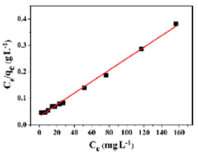	$\frac{C_e}{q_e} = \frac{1}{bq_m} + \frac{C_e}{q_m}$, $R_L = \frac{1}{1+bC_0}$ C_e is the concentration of Cu(II) at equilibrium; q_e is the amount of Cu(II) adsorbed at equilibrium; q_m is the maximum Langmuir monolayer adsorption capacity; b is the Langmuir constant; C_0 is the initial Cu(II) concentration; and R_L is a constant separation factor	410.72	0.07519	0.9956	0.1425

Model	Equation	Parameters		
		K	n	R^2
Freundlich 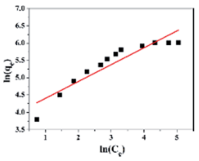	$\ln q_e = \frac{1}{n}\ln C_e + \ln K$ C_e and q_e are as above. K and $1/n$ are the characteristic Freundlich constants	49.91	2.05	0.8643

$$K_d = \frac{q_e}{C_e} \quad (5)$$

$$\ln K_d = \frac{\Delta S^\circ}{R} - \frac{\Delta H^\circ}{RT} \quad (6)$$

$$\Delta G^\circ = \Delta H^\circ - T\Delta S^\circ \quad (7)$$

where K_d is the distribution coefficient, T (K) is the absolute temperature, and R is the universal gas constant (8.314 J mol^{-1} K^{-1}). The values of ΔH° (kJ mol^{-1}) and ΔS° (kJ mol^{-1}) can be calculated from the slope and intercept of a plot of ln K_d *versus* $1/T$, as shown in Fig. 7. The thermodynamic parameters (ΔG°, ΔH° and ΔS°) are shown in Table S1.† The value of ΔH° is positive, which indicates that the adsorption process of the heavy metal on the adsorbent is endothermically driven. When $5 < \Delta H^\circ < 10$ kJ mol^{-1}, it denotes that the adsorption mechanism is physisorption; when $30 < \Delta H^\circ < 70$ kJ mol^{-1}, the adsorption mechanism is chemisorption. As shown in Table S1,† the value of ΔH° (36.607 kJ mol^{-1}) indicated that chemical adsorption was the major process involved in the adsorption of Cu(II) on the CFO@SiO_2–NH_2 magnetic adsorbent. In addition, the value of ΔS° was also positive owing to the complexation of amino groups on the surface of the nanospheres with more mobile metal ions, which would cause an increase in entropy during the adsorption process. Furthermore, the ΔG° values at 298 K, 308 K, 318 K and 328 K were −3.098, −4.431, −5.763 and −7.096 kJ mol^{-1}, respectively. A negative value of ΔG° indicates that the adsorption process is spontaneous. It also reveals that

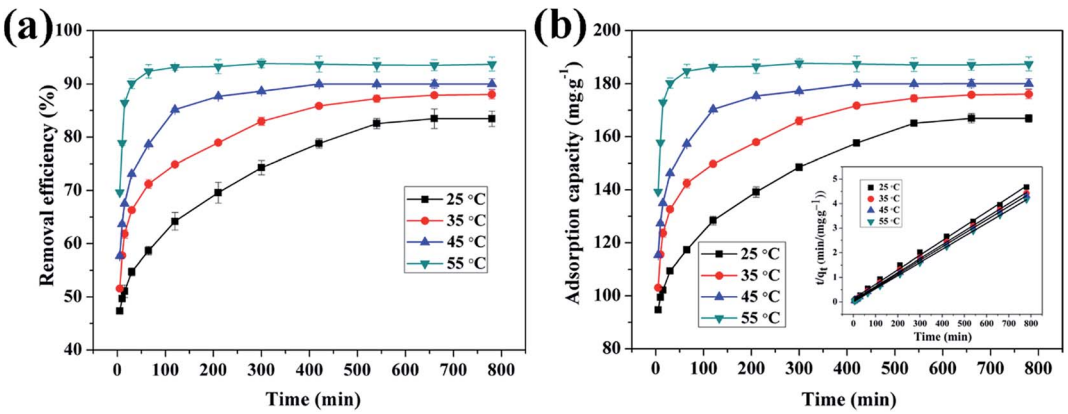

Fig. 6 Effect of contact temperature on adsorption of Cu(II) by CFO@SiO_2–NH_2: (a) removal efficiency, (b) adsorption capacity, and (inset of (b)) pseudo-second-order kinetics plots.

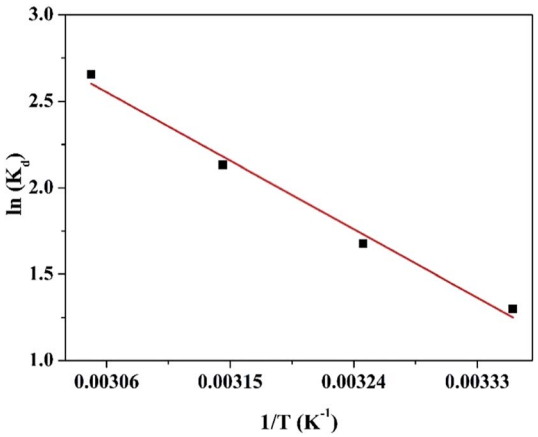

Fig. 7 Linear dependence of ln K_d on 1/T based on the adsorption thermodynamics.

a more negative ΔG° value reflects a greater driving force of adsorption, which results in faster adsorption performance and a higher adsorption capacity. The results were also fitted with the above discussion (Fig. 6).

3.4.4 Effect of reaction time on adsorption of Cu(II), Cd(II) and Pb(II) ions by CFO@SiO_2–NH_2. The contact time between the adsorbent and adsorbate is also an important parameter that plays a vital role in the adsorption process. Fig. 8 shows the adsorption of Cu(II), Cd(II), and Pb(II) ions on CFO@SiO_2–NH_2 as a function of the contact time. The adsorption tendency of the three ions was similar. The removal efficiency for Cu(II) and Cd(II) rose sharply within the initial 60 min and then increased slowly for another 240 min. Finally, it remained constant even when the contact time was extended to 780 min (Fig. 8a). Furthermore, the adsorption of Pb(II) on CFO@SiO_2–NH_2 reached equilibrium after 30 min, which was faster than Cu(II) and Cd(II). The rapid adsorption rate during the initial stages may mainly be attributed to the unique complexation between the heavy metal ions and the amine functionalities of the SiO_2 shell on $CoFe_2O_4$ NPs. The adsorption capacities of CFO@SiO_2–NH_2 for Cd(II), Cu(II) and Pb(II) were 199.9, 177.8 and 181.6 mg g^{-1}, respectively (Fig. 8b), which were comparable to the best reported value. The adsorption capacities for Cd(II), Cu(II) and Pb(II) of other representative materials are summarized in Table 2.[23,31,36,57,58]

3.4.5 Study of adsorption kinetics. To study the mechanism of adsorption kinetics in depth, two well-known adsorption models, namely, the pseudo-first-order and pseudo-second-order kinetics models, were used to investigate the dynamics of the adsorption process. It was found that the pseudo-second-order model fits the adsorption of heavy metal ions on CFO@SiO_2–NH_2 better than the pseudo-first-order model. The pseudo-second-order equation is eqn (8):

$$\frac{t}{q_t} = \frac{1}{k_2 q_e^2} + \frac{t}{q_e} \quad (8)$$

where q_e and q_t (mg g^{-1}) are the adsorption capacities at equilibrium and time t, respectively, and k_2 in eqn (8) is the pseudo-second-order rate constant (g mg^{-1} min^{-1}). Linear fits based on eqn (8) have been plotted in the insets of Fig. 4b, 6b and 8b, respectively. The calculated kinetics parameters and correlation coefficients (R^2) are given in Table 3. The best fit of the pseudo-second-order model suggests that a chemisorption mechanism was involved in the adsorption,[59,60] which is further supported by the adsorption thermodynamics (Section 3.4.3). Furthermore, small differences between the experimental (q_e (exp.)) and calculated (q_e (cal.)) values of the equilibrium adsorption capacity were also observed, and the pseudo-second-order model gave a better fit with the experimental data (Table 3).

3.5 Regeneration and recyclability

The recyclability of adsorbents is highly important for their practical application. On the basis of the analysis of the effect of pH on the adsorption of heavy metal ions, we adopted the method of acid treatment to regenerate the adsorbent. Fig. 9 shows the removal efficiency of CFO@SiO_2–NH_2 nanospheres for the adsorption of Cd(II), Cu(II) and Pb(II) after five stages of recycling. The removal efficiency in the first cycle was found to be 99.85%, 87.80% and 90.10%, respectively. The adsorption capacities slightly decreased with an increase in the number of

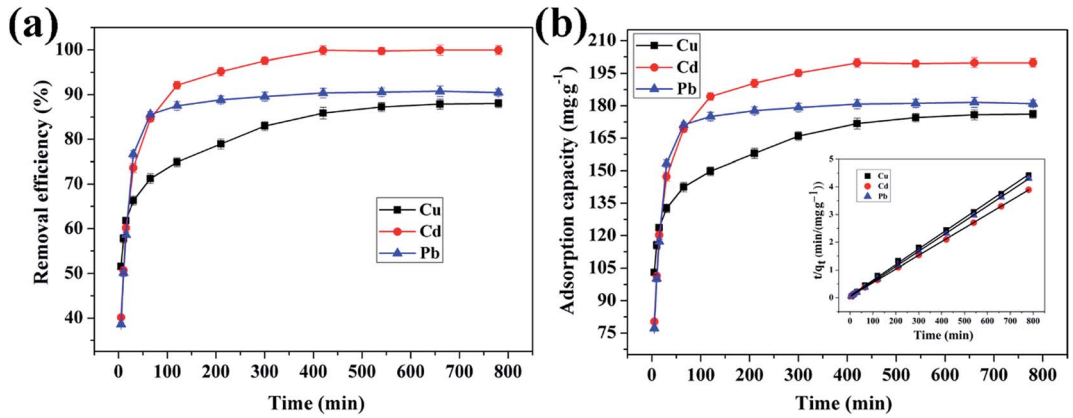

Fig. 8 Effect of contact time on adsorption of heavy metal ions (Cu(II), Cd(II), and Pb(II)) by CFO@SiO_2–NH_2: (a) removal efficiency, (b) adsorption capacity, and (inset of (b)) pseudo-second-order kinetics plots.

Table 2 Comparison of adsorption capacities of various adsorbents for Cd(II), Cu(II) and Pb(II) ions

Adsorbent	Adsorption capacity for heavy metal ions (mg g^{-1})			Ref.
	Cd(II)	Cu(II)	Pb(II)	
Modified magnetic mesoporous silica MCM-18	114.08	125.80	127.24	23
Sulfhydryl-functionalized hydrogel	17.7	9.3	31.3	57
Ni@$Mg(OH)_2$ core–shell nanocomposites	44.98	40.18	—	31
Amino-functionalized Fe_3O_4@SiO_2 magnetic nanomaterial	—	29.9	76.7	36
Magnetic Fe_3O_4 baker's yeast biomass	22.5	—	88.2	58
CFO@SiO_2–NH_2 nanospheres	199.9	177.8	181.6	Present work

Table 3 Parameters of pseudo-second-order kinetics model for the adsorption of Cu(II), Cd(II) and Pb(II) on CFO@SiO_2–NH_2

Metal	pH	Temperature (°C)	Removal efficiency (%)	q_e (exp.) (mg g^{-1})	k_2 (g mg^{-1} min^{-1})	q_e (cal.) (mg g^{-1})	R^2
Cu(II)	7	35	88.05 ± 0.838	177.8 ± 1.675	0.000401	178.891	0.99897
Cd(II)			99.95 ± 0.989	199.9 ± 1.978	0.000453	201.252	0.99994
Pb(II)			90.79 ± 1.184	181.6 ± 2.367	0.000848	183.150	0.99997
Cu(II)	4	35	3.50 ± 0.672	7.0 ± 1.344	0.02043	6.922	0.99864
	6		74.50 ± 0.860	149.0 ± 1.719	0.000306	151.975	0.99747
	7		88.05 ± 0.838	177.8 ± 1.675	0.000401	178.891	0.99897
Cu(II)	7	25	83.47 ± 0.731	166.9 ± 1.462	0.000263	169.780	0.99683
		35	88.05 ± 0.838	177.8 ± 1.675	0.000401	178.891	0.99897
		45	90.00 ± 0.748	180.1 ± 1.495	0.000885	181.818	0.99940
		55	93.74 ± 1.288	187.5 ± 2.575	0.004364	187.617	0.99999

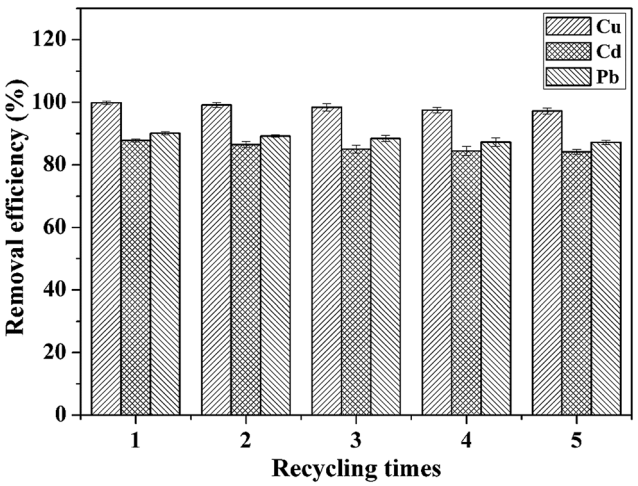

Fig. 9 Removal efficiency of CFO@SiO_2–NH_2 for the adsorption of different heavy metal ions over five cycles of use.

cycles: after four cycles of adsorption, the adsorption efficiency for Cd(II), Cu(II) and Pb(II) was around 97.25%, 84.15% and 87.12%, respectively. This indicates that the adsorbent can be used at least five times with high adsorption efficiency. It can be deduced that the CFO@SiO_2–NH_2 magnetic adsorbent has excellent desorption ability and can be recycled easily from wastewater using a magnetic field owing to its good magnetic response. All these conclusions illustrate that the CFO@SiO_2–NH_2 core–shell nanospheres can be used as a high-performance adsorbent for application in the field of removal of heavy metal ions.

4 Conclusions

In summary, a monodisperse amino-functionalized magnetic $CoFe_2O_4$@SiO_2 nanosphere was successfully fabricated. The sphere had a core–shell structure with a magnetic $CoFe_2O_4$ core (~10 nm), a non-porous silica layer (~35 nm) and an amino-functionalized layer. The monodisperse nanosphere can graft many more amino groups, which can improve its adsorption performance for heavy metal ions. The effects of the pH, initial concentration, reaction temperature and time on the adsorption of heavy metal ions by $CoFe_2O_4$@SiO_2–NH_2 were analyzed systematically. The adsorption process on the nanospheres was well described by the Langmuir model, and the adsorption kinetics can be best fitted by the pseudo-second-order kinetics model. Analysis of a thermodynamic study of Cu(II) showed that the process of adsorption was spontaneous and endothermic in nature. After acid treatment, the as-synthesized adsorbent could be regenerated and reused for up to five cycles with high chemical stability. The superparamagnetism possessed by the adsorbent makes it easy to remove from the reaction system. Therefore, the monodisperse nanospheres can be employed as an adsorbent with excellent performance in the field of the removal of heavy metal ions.

Acknowledgements

This work was supported by the National High-Tech Research and Development Program of China (863 Program) (No. 2015AA034701) and the Fundamental Research Funds for the Central Universities (No. 2008QNA4008).

References

1 F. Fu and Q. Wang, *J. Environ. Manage.*, 2011, **92**, 407–418.
2 M. Hua, S. Zhang, B. Pan, W. Zhang, L. Lv and Q. Zhang, *J. Hazard. Mater.*, 2012, **211–212**, 317–331.
3 V. K. Gupta, I. Ali, T. A. Saleh, A. Nayak and S. Agarwal, *RSC Adv.*, 2012, **2**, 6380–6388.
4 D. Kolodyńska, M. Kowalczyk and Z. Hubicki, *J. Mater. Sci.*, 2014, **49**, 2483–2495.
5 D. Vilela, J. Parmar, Y. F. Zeng, Y. L. Zhao and S. Sánchez, *Nano Lett.*, 2016, **16**, 2860–2866.
6 C. J. Madadrang, H. Y. Kim, G. Gao, N. Wang, J. Zhu, H. Feng, M. Gorring, M. L. Kasner and S. Hou, *ACS Appl. Mater. Interfaces*, 2012, **4**, 1186–1193.
7 C. T. Nguyen, P. Loganathan, T. V. Nguyen, S. Vigneswaran, J. Kandasamy and R. Naidu, *Chem. Eng. J.*, 2015, **270**, 393–404.
8 E. Eren, *J. Hazard. Mater.*, 2008, **159**, 235–244.
9 T. Phuengprasop, J. Sittiwong and F. Unob, *J. Hazard. Mater.*, 2011, **186**, 502–507.
10 A. T. Paulino, L. A. Belfiore, L. T. Kubota, E. C. Muniz, V. C. Almeida and E. B. Tambourgi, *Desalination*, 2011, **275**, 187–196.
11 L. Tang, G. M. Zeng, G. L. Shen, Y. P. Li, Y. Zhang and D. L. Huang, *Environ. Sci. Technol.*, 2008, **42**, 1207–1212.
12 K. A. Krishnan, *Colloids Surf., A*, 2008, **317**, 344–351.
13 C. S. Sundaram, N. Viswanathan and S. Meenakshi, *J. Hazard. Mater.*, 2009, **163**, 618–624.
14 L. M. Nikolenko, A. V. Ivanchihina, S. B. Brichkin and V. F. Razumov, *J. Colloid Interface Sci.*, 2009, **332**, 366–372.
15 S. A. Cetinus, E. Sahin and D. Saraydin, *Food Chem.*, 2009, **114**, 962–969.
16 V. Asokbunyarat, E. D. van Hullebusch, P. N. L. Lens and A. P. Annachhatre, *Water, Air, Soil Pollut.*, 2015, **226**, 143.
17 D. V. Quang, J. K. Kim, P. B. Sarawade, D. H. Tuan and H. T. Kim, *J. Ind. Eng. Chem.*, 2012, **18**, 83–87.
18 R. D. Ambashta and M. Sillanpää, *J. Hazard. Mater.*, 2010, **180**, 38–49.
19 Y. Q. Tan, M. Chen and Y. M. Hao, *Chem. Eng. J.*, 2012, **191**, 104–111.
20 H. V. Tran, L. D. Tran and T. N. Nguyen, *Mater. Sci. Eng., C*, 2010, **30**, 304–310.
21 X. Chen, K. F. Lam and K. L. Yeung, *J. Chem. Eng. Data*, 2011, **172**, 728–734.
22 C. T. Yavuz, A. Prakash, J. T. Mayo and V. L. Colvin, *Chem. Eng. Sci.*, 2009, **64**, 2510–2521.
23 M. Anbia, K. Kargosha and S. Khoshbooei, *Chem. Eng. Res. Des.*, 2015, **93**, 779–788.
24 F. Zhang, J. Lan, Z. S. Zhao, Y. Yang, R. Q. Tan and W. J. Song, *J. Colloid Interface Sci.*, 2012, **387**, 205–212.
25 Q. Q. Qu, L. Zhou, S. G. Zhao, H. J. Geng, J. J. Hao, Y. Y. Xu, H. L. Chen and X. G. Chen, *Chem. Eng. J.*, 2012, **180**, 121–127.
26 M. F. Shao, F. Y. Ning, J. W. Zhao, M. Wei, G. E. David and X. Duan, *J. Am. Chem. Soc.*, 2012, **134**, 1071–1077.
27 S. Venkateswarlu and M. Yoon, *ACS Appl. Mater. Interfaces*, 2015, **7**, 25362–25372.
28 Z. U. Rahman, Y. L. Dong, L. Su, Y. H. Ma, H. J. Zhang and X. G. Chen, *Chem. Eng. J.*, 2013, **222**, 382–390.
29 Y. M. Liu, X. J. Ju, Y. Xin, W. C. Zhang, W. Wang, J. Wei, R. Xie, Z. Liu and L. Y. Chu, *ACS Appl. Mater. Interfaces*, 2014, **6**, 9530–9542.
30 T. Wu, Y. Liu, X. Zeng, T. T. Cui, Y. T. Zhao, Y. N. Li and G. X. Tong, *ACS Appl. Mater. Interfaces*, 2016, **8**, 7370–7380.
31 M. Zhang, W. Q. Song, Q. L. Chen, B. J. Miao and W. C. He, *ACS Appl. Mater. Interfaces*, 2015, **7**, 1533–1540.
32 C. Q. Yang, G. Wang, Z. Y. Lu, J. Sun, J. Q. Zhuang and W. S. Yang, *J. Mater. Chem.*, 2005, **15**, 4252–4257.
33 A. L. Morel, S. I. Nikitenko, K. Gionnet, A. Wattiaux, J. Lai-Kee-Him, C. Labrugere, B. Chevalier, G. Deleris, C. Petibois, A. Brisson and M. Simonoff, *ACS Nano*, 2008, **2**, 847–856.
34 Z. J. Xu, W. Li, Z. D. Xiong, J. L. Fang, Y. G. Li, Q. Wang and Q. F. Zeng, *Desalin. Water Treat.*, 2015, **57**, 7054–7065.
35 N. M. Mahmoodi, S. Khorramfar and F. Najafi, *Desalination*, 2011, **279**, 61–68.
36 J. H. Wang, S. R. Zheng, Y. Shao, J. L. Liu, Z. Y. Xu and D. Q. Zhu, *J. Colloid Interface Sci.*, 2012, **387**, 205–212.
37 J. M. Zhang, S. R. Zhai, B. Zhai, Q. D. An and G. Tian, *J. Sol-Gel Sci. Technol.*, 2012, **64**, 347–357.
38 J. M. Zhang, S. R. Zhai, S. Li, Z. Y. Xiao, Y. Song, Q. D. An and G. Tian, *Chem. Eng. J.*, 2013, **215–216**, 461–471.
39 Q. Yuan, N. Li, Y. Chi, W. C. Geng, W. F. Yan, Y. Zhao, X. T. Li and B. Dong, *J. Hazard. Mater.*, 2013, **254–255**, 157–165.
40 G. Jacintho, A. G. Brolo, P. Corio, P. Suarez and J. C. Rubim, *J. Phys. Chem. C*, 2009, **113**, 7684–7691.
41 D. Tang, R. Yuan, Y. Chai and H. An, *Adv. Funct. Mater.*, 2007, **17**, 976–982.
42 X. Z. Ren, J. H. Shi, L. Z. Tong, Q. H. Li and H. Yang, *J. Nanopart. Res.*, 2013, **15**, 1–10.
43 L. J. Zhao, H. J. Zhang, L. Zhou, Y. Xing, S. Y. Song and Y. Q. Lei, *Chem. Commun.*, 2008, **30**, 3570–3572.
44 J. Hu, I. M. C. Lo and G. H. Chen, *Sep. Purif. Technol.*, 2007, **56**, 249–256.
45 F. B. Zhao, Y. C. Zou, X. J. Lv, H. W. Liang, Q. Jia and W. K. Ning, *J. Chem. Eng. Data*, 2015, **60**, 1338–1344.
46 B. Viltužnik, A. Košak, Y. L. Zub and A. Lobnik, *J. Sol-Gel Sci. Technol.*, 2013, **68**, 365–373.
47 B. Viltužnik, A. Lobnik and A. Košak, *J. Sol-Gel Sci. Technol.*, 2015, **74**, 199–207.
48 C. R. Ren, X. G. Ding, H. Q. Fu, C. Meng, J. C. Zhao, W. Q. Li and H. Yang, *RSC Adv.*, 2016, **6**, 72479–72486.
49 L. Sun, Y. X. Li, M. D. Sun, H. G. Wang, S. F. Xu, C. Q. Zheng and Q. B. Yang, *New J. Chem.*, 2011, **35**, 2697–2704.
50 L. L. Yang, P. Zou, J. Cao, Y. F. Sun, D. L. Han, S. Yang, G. Chen, X. W. Kong and J. H. Yang, *Superlattices Microstruct.*, 2014, **76**, 205–212.
51 Q. Chang, L. Zhu, C. Yu and H. Tang, *J. Lumin.*, 2008, **128**, 1890–1895.
52 Q. Wang, W. Gao, Y. Liu, J. Yuan, Z. Xu, Q. Zeng and Y. Li, *Chem. Eng. J.*, 2014, **250**, 55–65.
53 A. A. Atia, A. M. Donia and W. A. Al-Amrani, *Chem. Eng. J.*, 2009, **150**, 55–62.

54 S. Lan, X. Wu, L. Li, M. Li, F. Guo and S. Gan, *Colloids Surf., A*, 2013, **425**, 42–50.
55 A. M. Donia, A. A. Atia, W. A. Al-amrani and A. M. El-Nahas, *J. Hazard. Mater.*, 2009, **161**, 1544–1550.
56 Z. F. Jiang, J. M. Xie, D. L. Jiang, Z. X. Yan, J. J. Jing and D. Liu, *Appl. Surf. Sci.*, 2014, **292**, 301–310.
57 R. Hua and Z. K. Li, *Chem. Eng. J.*, 2014, **249**, 189–200.
58 M. Xu, Y. S. Zhang, Z. M. Zhang, Y. O. Shen, M. J. Zhao and G. T. Pan, *Chem. Eng. J.*, 2011, **168**, 737–745.
59 E. Rosales, M. Pazos, M. A. Sanromán and T. Tavares, *Desalination*, 2012, **284**, 150–156.
60 S. Wang, J. Wei, S. S. Lv, Z. Y. Guo and F. Jiang, *Clean: Soil, Air, Water*, 2013, **41**, 992–1001.